Accelerated separation of photogenerated charge carriers and enhanced photocatalytic performance of g-C$_3$N$_4$ by Bi$_2$S$_3$ nanoparticles

Qiang Hao,[a,b,1] Ci'an Xie,[a,1] Yongming Huang,[a] Daimei Chen,[a]* Yiwen Liu,[b] Wei Wei,[b] Bing-Jie Ni[b#]

a: Beijing Key Laboratory of Materials Utilization of Nonmetallic Minerals and Solid Wastes, School of Materials Science and Technology, China University of Geosciences Beijing, Beijing, 100083, China
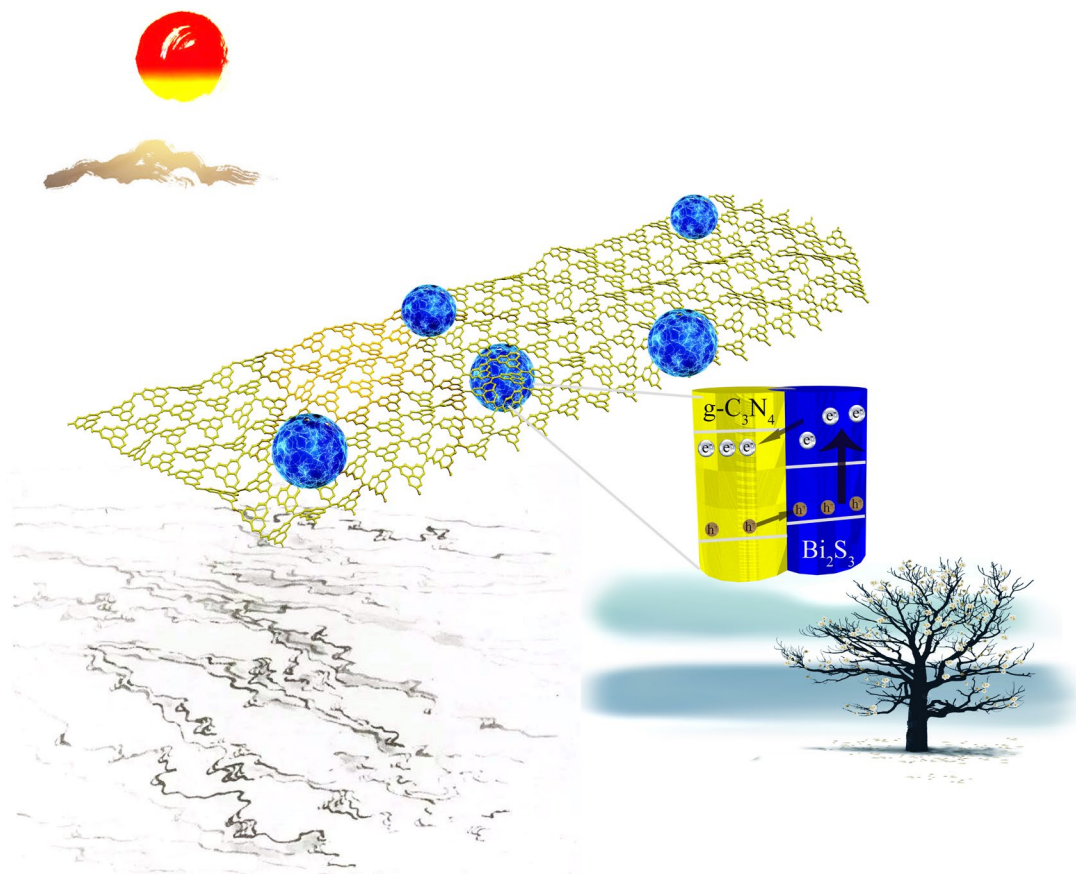
b: Centre for Technology in Water and Wastewater (CTWW), School of Civil and Environmental Engineering, University of Technology Sydney (UTS), Sydney, NSW 2007, Australia

1: These authors contributed the same to this manuscript

*Corresponding author: chendaimei@cugb.edu.cn

[#] Corresponding author: Tel.: +61 295147401; E-mail: bingjieni@gmail.com

TOC

g-C$_3$N$_4$

Bi$_2$S$_3$

Abstract

Employing photothermal conversion to improve the photocatalytic of g-C_3N_4 is rarely reported previously. Herein, different ratios of g-C_3N_4/Bi_2S_3 heterojunction materials are synthesized by a facile ultrasonic method. Advanced characterizations such as X-ray Diffraction (XRD), Fourier transform infrared spectroscopy (FTIR), X-ray photoelectron spectroscopy (XPS) and high-resolution transmission electron microscopy (HRTEM) are employed to analyze the morphology and structure of the prepared materials. Compare with sole counterparts, the heterojunction materials CN-BiS-2 exhibit significantly enhanced photocatalytic performance, which is 2.05 time as g-C_3N_4 and 4.42 times as Bi_2S_3. A possible degradation pathway of methylene blue (MB) was proposed. Based on the photoproduced high-energy electrons and photothermal effect of Bi_2S_3, the transfer and separation of electron-hole pairs are greatly enhanced and more active species are produced. In addition, the relatively high utilization efficiency of solar energy has synergistic effect for the better photocatalytic performance.

Keywords: Graphitic carbon nitride; Bismuth sulfide; Photocatalyst; Wastewater treatment; high-energy electron

1. Introduction

Photocatalytic technology is a kind of advanced oxidation technology, which uses light to excite electrons to produce highly oxidizing species.[1-4] It can mineralize

organic molecules to carbon dioxide and water, thus eliminating organic pollutants from water completely.[5, 6] Traditional photocatalyst such as titanium dioxide (TiO_2), zinc oxide (ZnO) and bismuth phosphate ($BiPO_4$) have outstanding photocatalytic performance for water splitting and/or organic pollutant degradation.[7-10] However, their application is highly limited by their wide bandgap (e.g., 3.2 eV, that can only be excited by UV light) and low utilization ratio of solar energy (i.e., UV light accounts for about only 4% of solar light).[11]

In recent years, visible light response photocatalysts arise increasing interests. A series of new photocatalyst such as bismuth oxide (Bi_2O_3),[12-14] bismuth vanadate ($BiVO_4$),[15, 16] cadmium sulfide (CdS),[17, 18] ferric oxides (Fe_2O_3)[19, 20] or graphitic carbon nitride (g-C_3N_4)[21-23] were developed to overcome the shortages of UV light response photocatalysts. Among these semiconductors, g-C_3N_4 attracted extreme attentions due to its advantages of metal-free, wide resource, nontoxic and facile preparation.[24-27] However, the bandgap of g-C_3N_4 is about 2.7 eV, which means that it can only absorb the light lower than 460 nm and its utilization ratio of solar light is still not high.[28, 29] In addition, the rapid recombination of photogenerated charge carriers is another aspect limiting the application of g-C_3N_4.[30]

Constructing heterojunctions with other semiconductors is an efficient way to improve the photocatalytic performance of g-C_3N_4. Several g-C_3N_4 based heterojunctions such as BiOCl/g-C_3N_4, TiO_2/g-C_3N_4, Bi_2MoO_6/g-C_3N_4, Al_2O_3/g-C_3N_4, Ag_3PO_4/g-C_3N_4 have been developed previously, nevertheless, the poor light absorption is still limiting their application.[31-35] Therefore, better g-C_3N_4 based

heterojunction materials should be synthesized to facilitate its high-efficient application. Sulfur-based materials have been widely used to improve the performance of photocatalysts.[36-39] Bismuth sulfide (Bi_2S_3) is the main component of bismuth glance that belongs to orthorhombic crystal system with a narrow-bandgap of 1.3 – 1.7 eV.[40] Because of its distinctive electron structure and optical property, Bi_2S_3 has wide application prospect in different areas such as photocatalyst,[41, 42] photodetector[43, 44] or medical imaging.[45] Due to the Peltier effect of Bi_2S_3, it can be used in thermoelectric-cooling technologies.[46, 47] The excellent photothermal conservation effect also make Bi_2S_3 a unique material in photothermal cancer treatment.[48, 49]

In fact, combining Bi_2S_3 with g-C_3N_4 to create heterojunction has been demonstrated to be a highly efficient way to improve the photocatalytic activity of g-C_3N_4. However, the reported methods in literature are rather complicated. For instance, Xuan et al. used the microwave-assisted method to prepare g-C_3N_4/Bi_2S_3, in which microwave oven and nitrogen must be used.[50] Chen et al. put g-C_3N_4 and the precursor of Bi_2S_3 in a Teflon-lined steel autoclave and heated it at 160 °C for 30 h. After that, the product was collected, washed and dried in a vacuum oven. The final product includes g-C_3N_4/Bi_2S_3 and Bi.[51] Yin et al. reported another method to prepare g-C_3N_4/Bi_2S_3 composite materials, through calcining the mixture of ammonium thiocyanate (NH_4SCN) and bismuth chloride ($BiCl_3$) at 550 °C in nitrogen atmosphere.[52] In addition, the potential mechanisms for the enhanced photocatalytic activity of g-C_3N_4/Bi_2S_3 heterojunctions in these previous studies remained unclear or

even contradictory. In particular, Xuan et al. claimed that the enhanced separation of electron and hole pairs should be assigned to the transfer of electrons rather than holes[45]. In contrast, Chen et al. stated that the transfer of holes should be the key reason for the better photocatalytic performance[46]. Thus, the questions remained to be answered include: Can g-C_3N_4/Bi_2S_3 heterojunctions be synthesized more facilely? How does Bi_2S_3 influence the photocatalytic performance of g-C_3N_4? What is the transfer path of electrons and holes?

Herein, we employed a facile coprecipitation method to prepare Bi_2S_3 at low temperature. Bi_2S_3 was induced to g-C_3N_4 nanosheets by ultrasonic and the obtained g-C_3N_4/Bi_2S_3 heterojunctions exhibited better photocatalytic performance than g-C_3N_4 nanosheets and Bi_2S_3 particles. The morphology and structure of the prepared materials are comprehensively characterized. The potential mechanisms for the enhanced catalytic performance are then analyzed. The findings of this work are expected to provide insights into the synthesis and application of g-C_3N_4 based heterojunction photocatalysts.

2. Experimental section

2.1 Reagents

Bismuth ammonium citrate was bought form Tianjin Guangfu Fine Chemical Research Institute. Thioacetamide and melamine were bought from Sinopharm Chemical Reagent Beijing Co., Ltd. All the chemicals were analytical reagent and used without further purification.

2.2 Preparation of materials

g-C$_3$N$_4$ nanosheets were prepared as follow. Firstly, 2 g of melamine was located in a 50 mL corundum crucible and heated to 540 °C for 4 h. The heating rate was 4 °C/min and the atmosphere was air. After that, the product (bulk g-C$_3$N$_4$) was ground uniformly and reheated at 500 °C for 2 h in air. Then g-C$_3$N$_4$ nanosheets are obtained.[53]

Bi$_2$S$_3$ was synthesized by using the coprecipitation method. Firstly, 30 mL of bismuth ammonium citrate solution (0.0075 M) and 30 mL of thioacetamide solution (0.005 M) was put into two 100 mL flasks. Then the flasks were stirred for 10 min at 90 °C in water bath. After that, the thioacetamide solution was slowly added to the bismuth ammonium citrate solution. The mixture was kept at 90 °C for 2 h to form Bi$_2$S$_3$. Finally, the prepared Bi$_2$S$_3$ was washed by water and ethanol, and freeze-dried.

The g-C$_3$N$_4$/Bi$_2$S$_3$ heterojunctions were prepared by the ultrasonic method. The details are as follow: 1 g of g-C$_3$N$_4$ nanosheets, a certain amount of Bi$_2$S$_3$, 60 mL of water and 60 mL of ethanol were put in a 200 mL beaker. Then the mixture was strong stirred for 10 min and sonicated for 8 h. Afterwards, the powder was collected, washed 3 times and dried at 60 °C for 12 h. The amount of Bi$_2$S$_3$ was 2, 20 and 50 mg, besides, the samples were named as CN-BiS-1, CN-BiS-2 and CN-BiS-3 respectively.

2.3 Characterization of materials

The X-ray diffraction (XRD) of the samples was tested with a D/max-2400 X-ray diffractometer at 25 °C with intense Cu K_α radiation. A Bruker V70 Fourier transform infrared spectrometer was employed to test the Fourier transform infrared

spectroscopy (FTIR) of C_3N_4/Bi_2S_3 heterojunction samples and the wavenumber range

was from 4000 to 600 cm^{-1}. X-ray photoelectron spectroscopy (XPS) of the prepared

samples was obtained from a PHI Quantera XPS microprobe. JEOL2100F thermal

field high resolution scanning transmission electron microscope (STEM) with an

Oxford M-max 80 energy-dispersive X-ray spectroscopy (EDS) was used to explore

the morphology and structure of CN-BiS-2. The UV-vis diffuse reflectance

spectroscopy (DRS) of the samples was obtained from a Hitachi U-3900 scan UV–vis

spectrophotometer from 800 to 250 nm, the blank baseline of which was tested with

high purity barium sulfate ($BaSO_4$). Photoluminescence (PL) spectra were tested with

a Hitachi F-4600 fluorescence spectrometer excited at 325 nm and the wavelength

range was from 300 to 700 nm. The electrochemical impedance spectroscopy (EIS)

and photocurrent of the samples were tested by using a CHI 760E electrochemical

workstation. A platinum (Pt) wire was used as counter electrode, a saturated calomel

electrode (SCE) was used as reference electrode and the solution was 0.1 M sodium

sulfate (Na_2SO_4). The preparation of working electrodes was as fallow: 1 mL of water

and 5 mg of samples were put into 5 mL cuvettes; then the cuvettes were sonicated 4

h to disperse the samples in the solvent evenly; then the suspension was evenly coated

on indium-tin-oxide (ITO) glasses (5 × 2 cm) and dried in air for 12 h. The light

resource of photocurrent was provided by a 300 W xenon lamp (PLS-SXE-300) and

the light intensity was 50 mW/cm^2. The frequency of EIS was from 1 to 1×10^5 Hz;

the initial voltage was 0 V and the amplitude was 0.005 V. The electron spin

resonance (ESR) spectra of pure g-C_3N_4 and CN-BiS-2 were tested with a Bruker

ESR 300E spectrometer and *5,5*-dimethyl-*1*-pyrroline *N*-oxide (DMPO) was used as the radical scavenger. Thermal images were gained from Xinsite HT02 thermography with a 300 W Xe lamp (PLS-SXE300) irradiation.

2.4 Photocatalytic activity and product tests

Methylene blue (MB) was used as the molecular probes to evaluate the photocatalytic activity of the prepared samples. The photocatalytic reaction test was carried out with a PhchemIII photochemical reactions instrument and the light resource was a 500 W xenon lamp with average light intensity being 35 mW/cm^2. Firstly, 50 mg of the samples were weighted and located in five 50 mL quartz cuvettes. Then 50 mL of MB solution (5 ppm) was added to the cuvettes and the suspension was strong stirred for 2 h to reach the adsorption-desorption equilibrium. Afterwards, 3 mL of suspension was collected and the light was turned on. The photodegradation process lasted for 5 h and 3 mL of suspension was sampled per hour. The concentration of MB solution was measured with a Hitachi U-3900 scan UV–vis spectrophotometer at the wavelength of 664 nm. The total organic carbon (TOC) of the solutions during the photocatalytic degradation process was analyzed with a Shimadzu TOC-L. The degradation products were analyzed by a Shimadzu LCMS-8060 liquid chromatograph with tandem mass spectrometry (LCMSMS).

3. Results and discussion

3.1 Structure and morphology

Bi$_2$S$_3$ belongs to orthorhombic crystal system, crystallizing in the space group of

Pnma (62) with the unit cell parameters $a = 11.2690$ Å, $b = 3.9717$ Å, $c = 11.1290$ Å, and $Z = 4$.[54] Fig. 1 shows the crystal structure of Bi_2S_3. The formation of Bi_2S_3 presents a serrated chain-like structure, which is formed by the connection of the trigonal pyramid structure of $[Bi_2S_3]$. This structure grows along the (001) direction and two chains can connect with each other and form $[Bi_4S_6]_n$. The strong and short Bi–S in the chains are between 2.584 to 2.7439 Å, while the longer Bi–S between the chains are 3.056 Å.[55]
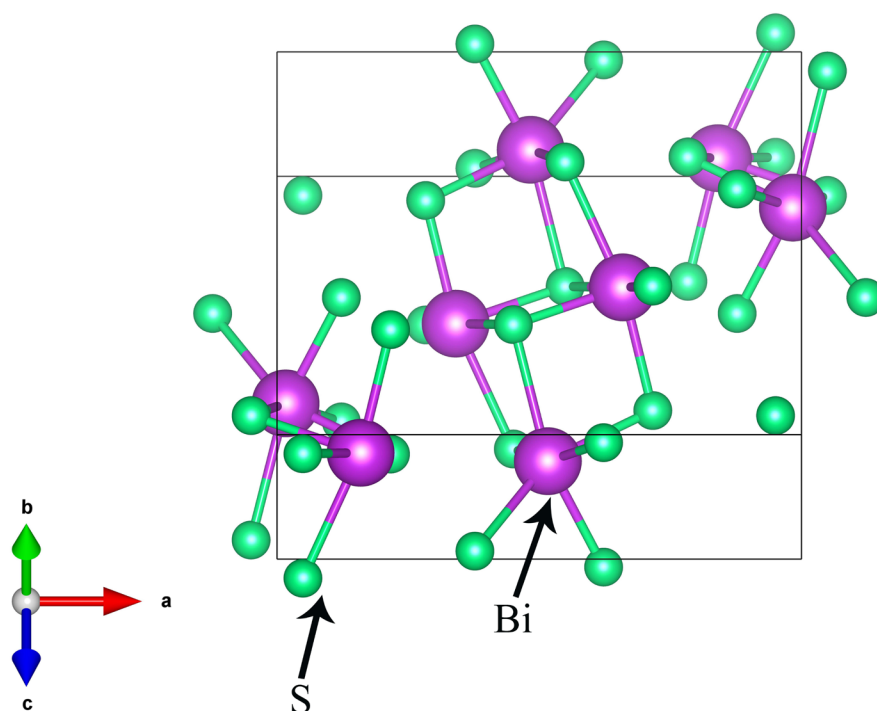
Fig. 1 The crystal structure of Bi_2S_3

Firstly, XRD patterns were used to explore the component and crystallinity of prepared materials. Fig. 2 is the XRD patterns of $g-C_3N_4$, Bi_2S_3 and $g-C_3N_4/Bi_2S_3$ heterojunction samples. The two peaks of $g-C_3N_4$ at 13.1 and 27.1° can be

attributed to the (100) and (002) crystal plane diffraction respectively (JCPDS 87-1526). The XRD pattern of Bi_2S_3 well matches the reference card (ICSD 153946) that has not strong crystallinity like g-C_3N_4. After sonicated with Bi_2S_3 in water and ethanol solution, the diffraction intensity of g-C_3N_4 gradually decreased, which illustrates that the crystallinity of the g-C_3N_4 was decreased. The effect of ultrasonic and solution can help further nanosize g-C_3N_4 and the Bi_2S_3 nanoparticles have a positive effect on the tailor of g-C_3N_4.[56, 57]
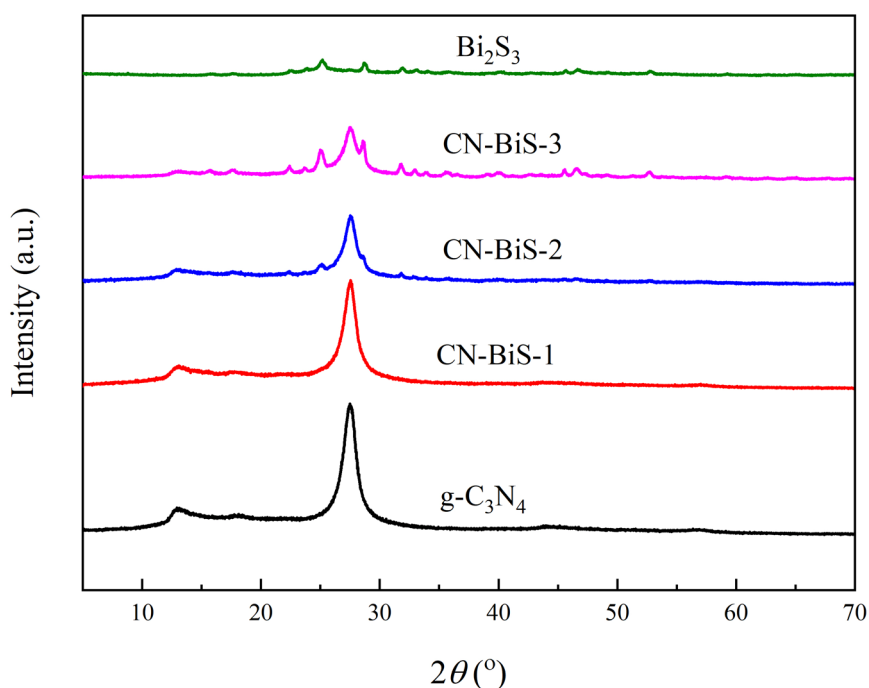
Fig. 2 XRD patterns of g-C_3N_4, Bi_2S_3 and g-C_3N_4/Bi_2S_3 heterojunction samples.

Afterwards, FTIR were employed to explore the surface functional groups of g-C_3N_4, Bi_2S_3 and g-C_3N_4/Bi_2S_3 samples (Fig. 3). The inorganic Bi_2S_3 had no obvious peaks in FTIR. For the g-C_3N_4 based samples, the wide peak at around 3400 cm^{-1} was attributed to the hydroxyl form water, which was adsorbed on the surface of the samples. The peaks at 1200, 1234, 1317 1457 and 1631 cm^{-1} were all assigned to the

skeletal vibration peaks of (C_6N_7).[58] The peak at 1400 cm^{-1} belonged to the stretching vibration of C_3N_3 and the vibration peaks of the out-of-plane skeleton of triazine rings showed a strong and sharp peak at 808 cm^{-1}.[59] Compared to g-C_3N_4, no new peak appears in the FTIR of g-C_3N_4/Bi_2S_3 samples, indicating that the interaction between g-C_3N_4 and Bi_2S_3 is physical interaction.
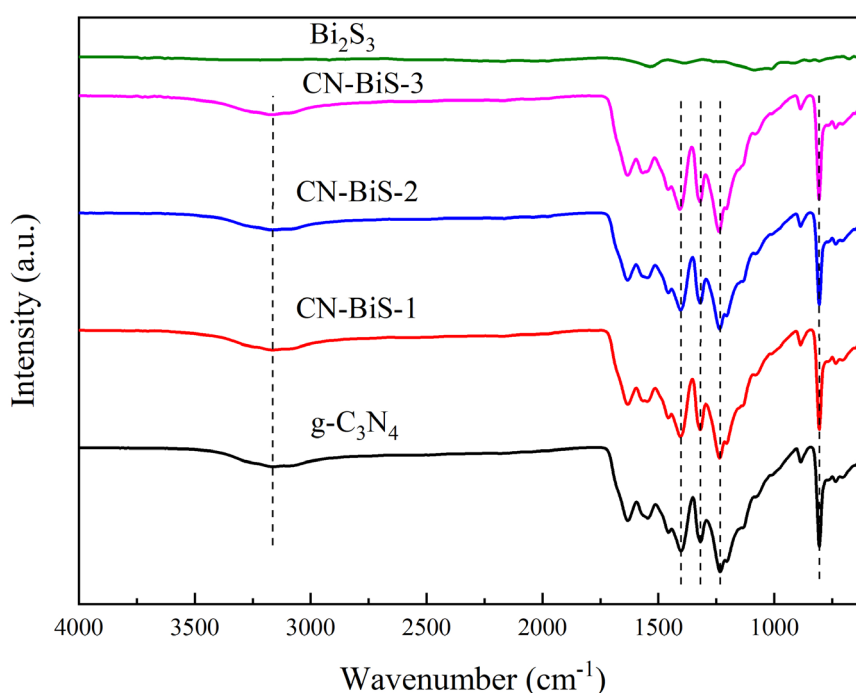
Fig. 3 FTIR of g-C_3N_4, Bi_2S_3 and g-C_3N_4/Bi_2S_3 heterojunction samples

Then, STEM and EDS mapping images were tested to explore the morphology and structure of CN-BiS-2. According to Fig. 4a, Bi_2S_3 particles (the bright part) in CN-BiS-2 were about 50 nm with irregular morphology. Some of the Bi_2S_3 particles were at the surface of g-C_3N_4 nanosheets, while the others were sandwiched in the g-C_3N_4 layers. As for g-C_3N_4, it showed a soft layer structure. The EDS mapping could further confirm the component and morphology of this sample.
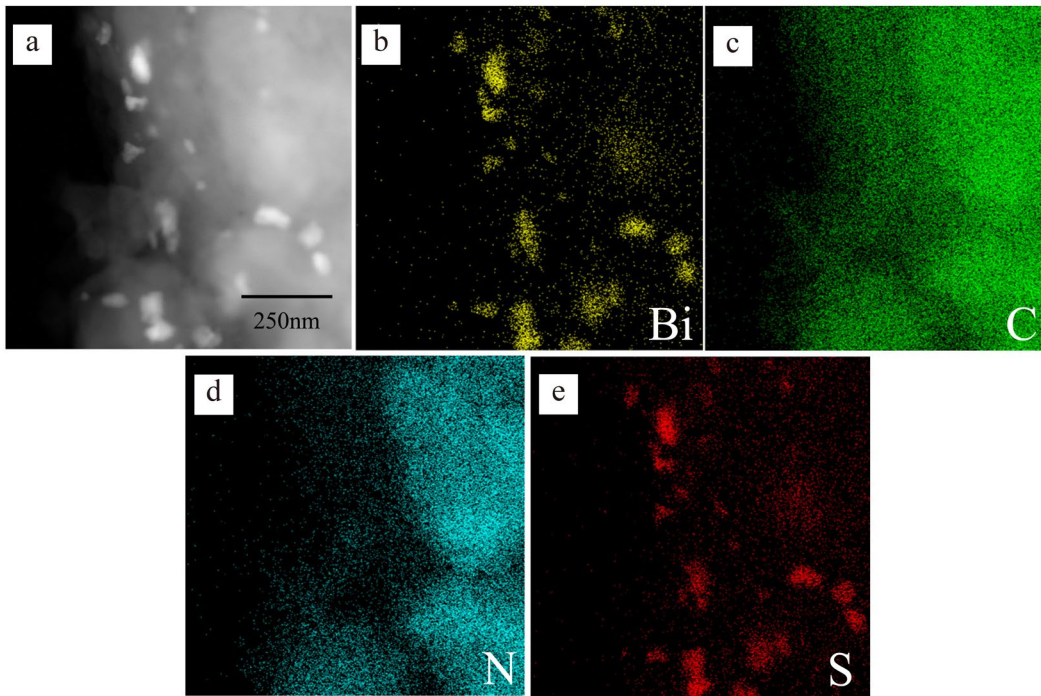
Fig. 4 STEM and EDS mapping images of CN-BiS-2; (a) the electron image and the EDS mapping images of Bi (b), C (c), N (d) and S (e).

Fig. 5a is the XPS narrow spectra of Bi and S of Bi_2S_3 and CN-BiS-2. For the low spectra intensity of CN-BiS-2, we enlarged this image and showed it in Fig. 5b. In Bi_2S_3, two distinct peaks at 163.6 and 158.3 eV can be assigned to the $4f_{5/2}$ and $4f_{7/2}$ of Bi^{3+}, respectively.[13] The weak peak at 160.1 eV is the $2p_{3/2}$ of S^{2-}.[60] For the peaks of Bi $4f_{5/2}$ and $4f_{7/2}$ of CN-BiS-2, the binding energy shifted to 163.2 and 157.9 eV, which is probably caused by the strong interaction between Bi_2S_3 and $g\text{-}C_3N_4$. As the concentration of Bi_2S_3 in sample CN-BiS-2 is quite low, it is difficult to judge the narrow spectra of S from this image. As shown in Fig. 5c, N1s has two peaks. The peak at 400.5 eV is attributed to the bridging N atoms in $N(C)_3$ or N bonded with H atoms. The other peak at 398.7 eV is assigned to the sp^2 hybridized N involved in triazine rings of $g\text{-}C_3N_4$. Due to the interaction between Bi_2S_3 and $g\text{-}C_3N_4$, the binding

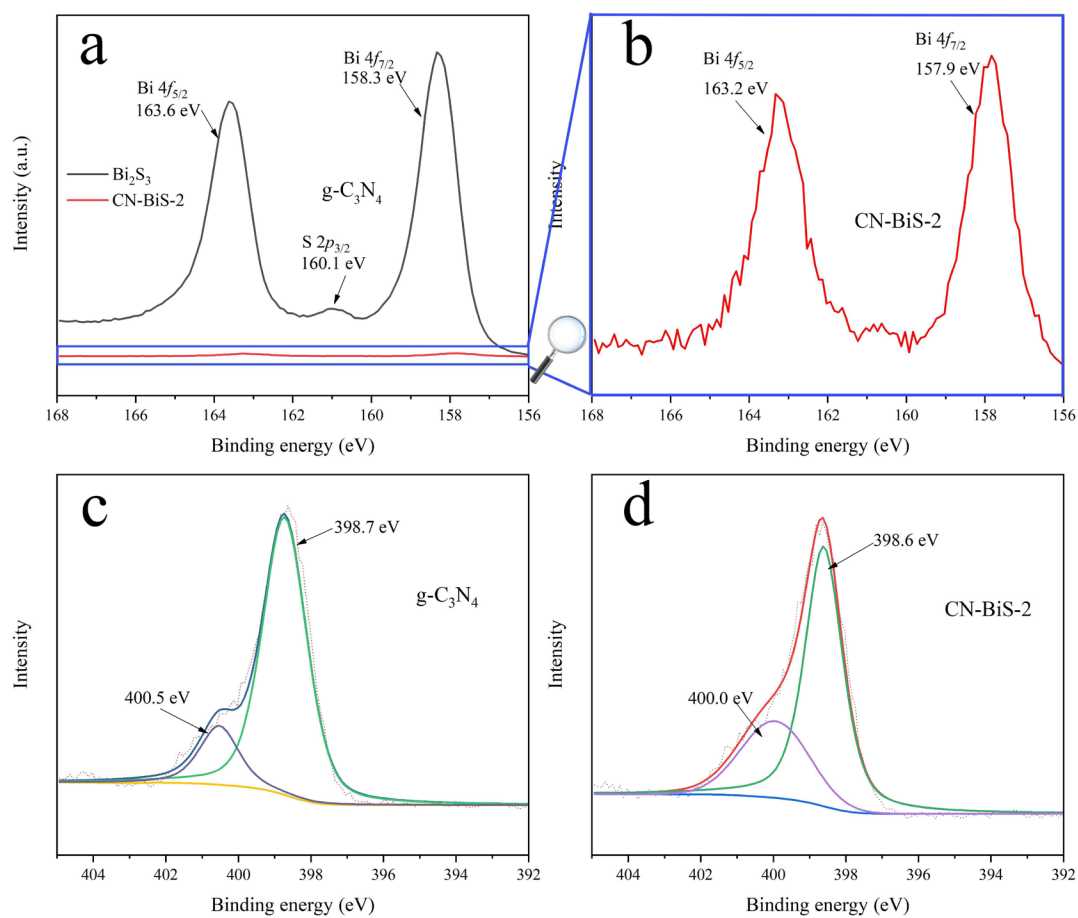energy of N1*s* peaks of CN-BiS-2 also showed some shift.

Fig. 5 XPS narrow spectra of (a) Bi and S of Bi_2S_3 and CN-BiS-2, (b) enlarged spectra of CN-BiS-2. XPS narrow spectra of N of (c) g-C_3N_4 and CN-BiS-2.

Based on the above results, we can conclude that g-C_3N_4/Bi_2S_3 heterojunction samples are successfully fabricated. The Bi_2S_3 particles were either at the surface of g-C_3N_4 nanosheets or sandwiched in the g-C_3N_4 layers. After sonicated with Bi_2S_3 in water and ethanol solution, the crystallinity of the g-C_3N_4 clearly decreased. The effect of ultrasonic and solution can further nanosize the g-C_3N_4 and the Bi_2S_3 nanoparticles have a positive effect on the tailor of g-C_3N_4.

3.2 Photocatalytic activity

MB was used as molecular probes to evaluate the photocatalytic activity of prepared samples. Fig. S1 shows the concentration change of MB under simulated solar light irradiation. It is obvious that the concentration of MB solution gradually decreased during the time course. Among all the samples, CN-BiS-2 had the highest photocatalytic activity and the total removal of MB is 92.11% in 6 h. The pseudo-first-order rate constant k of CN-BiS-2 is 0.521 h^{-1}, which is 2.05 time as g-C$_3$N$_4$ and 4.42 times as Bi$_2$S$_3$ (Fig. 6a). To further confirm the mineralization of MB, the TOC was tested. As shown in Fig. 6b, during 6 h, the TOC of MB reduced 82.03% by CN-BiS-2 and it is much higher than that of g-C$_3$N$_4$. However, the reduce of TOC is lower than the removal of MB concentration, indicating there are some intermediate and incompletely mineralized products. Then, LC-MSMS was employed to analyze the degradation products (Fig. S2) and a possible degradation path was proposed (Fig. 7). There are two major degradation pathways of MB by CN-BiS-2. Firstly, the oxygen in water can form S=O with MB.[61] Then a C–N is broken and 2,5-diamino-4-hydroxybenzenesulfinate was formed, which may be further degraded to ((2*E*,4*Z*)-5-amino-4-hydroxypenta-2,4-dien-2-yl) amide and 2,4-dimethylpent-2-en-3-ide. With increasing reaction time, these organic molecules can finally be converted to CO$_2$ and H$_2$O. In the other pathway, MB firstly lose two –CH$_3$ and then form 5λ^4-phenothiazin-3-ol. It may also be gradually mineralized by the photocatalytic active species.
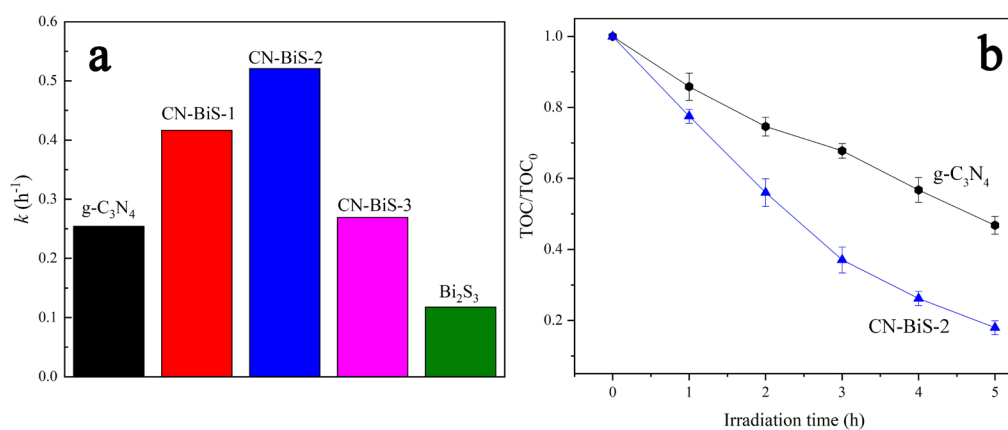
Fig. 6 Photocatalytic activity of g-C$_3$N$_4$, Bi$_2$S$_3$ and CN-BiS composite samples: (a) pseudo-first-order rate constant k., and (b) the TOC removal of g-C$_3$N$_4$ and CN-BiS-2.
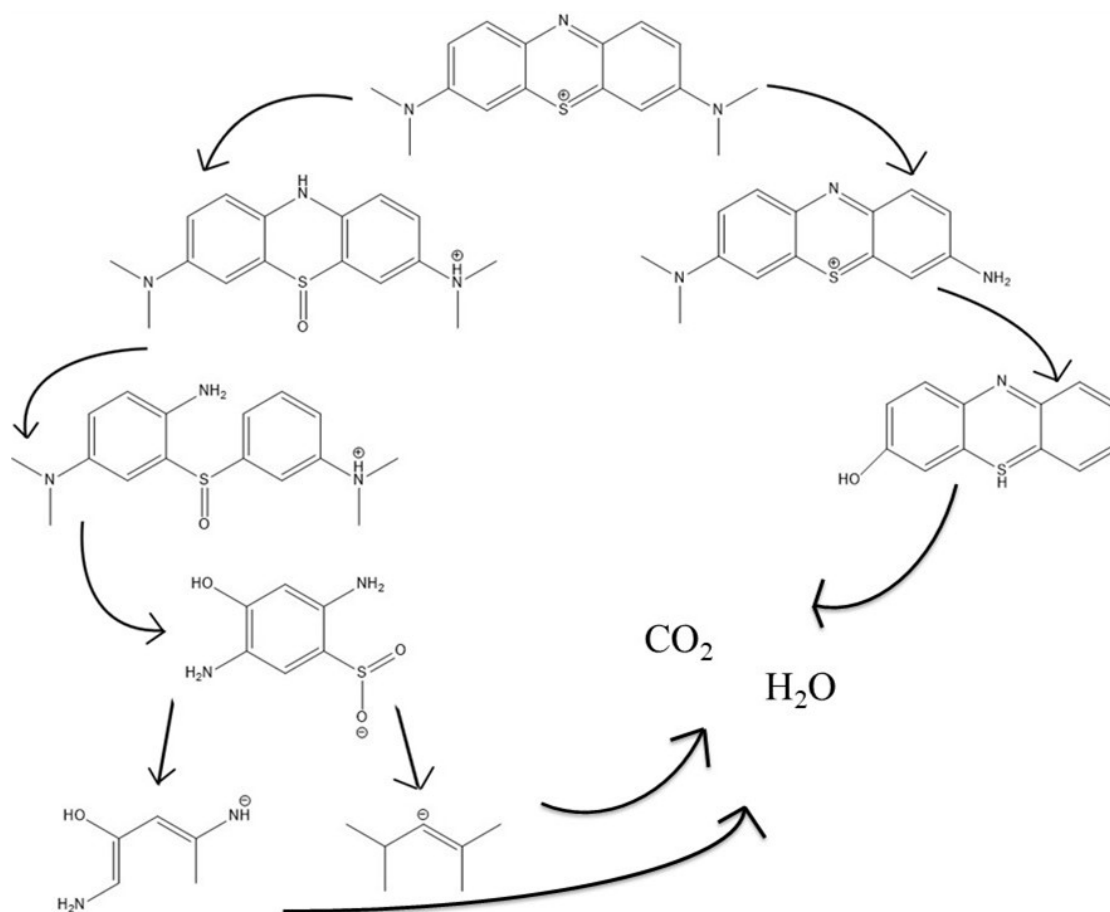

Fig.7 A possible degradation path of the methylene blue molecule.

3.3 Photocatalytic mechanism

Solar light utilization ratio has crucial influence on the application of

photocatalysts. Firstly, UV-vis DRS was employed to test the light absorption ability of prepared samples. Fig. 8 is the UV-vis DRS of g-C$_3$N$_4$, Bi$_2$S$_3$ and CN-BiS heterojunction samples. The g-C$_3$N$_4$ could only absorb the light lower than 460 nm and its bandgap was about 2.7 eV. When Bi$_2$S$_3$ was introduced to g-C$_3$N$_4$ nanosheets, the light absorption of the composite samples improved significantly both in the ultraviolet and visible light region. Besides, the absorption edges of the composite samples showed an obvious red-shift, which was caused by the strong interaction between g-C$_3$N$_4$ and Bi$_2$S$_3$. The wave-band absorption in the visible light region was also enhanced. The stronger light absorption can favor the samples to utilize more solar energy.
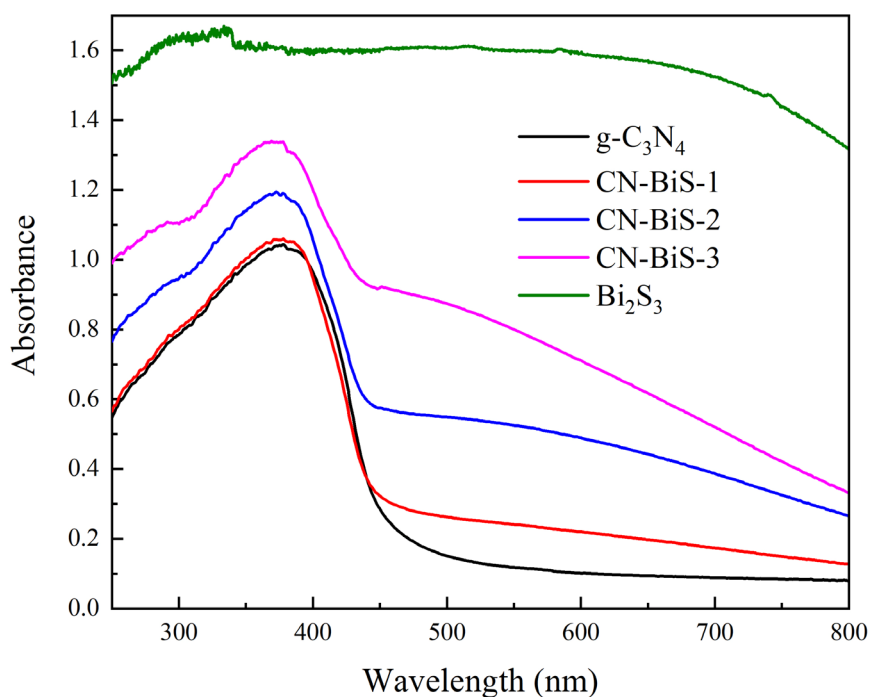

Fig. 8 UV-vis DRS of g-C$_3$N$_4$, Bi$_2$S$_3$ and CN-BiS composite samples

Photocurrent is an efficient way to prove the separation and transfer efficiency of

photogenerated charge carriers. Fig. 9a is the photocurrent of g-C_3N_4 and CN-BiS-2. It was obvious that both g-C_3N_4 and CN-BiS-2 have strong photocurrent response when the light was turned on. The photocurrent intensity of CN-BiS-2 was much higher than that of g-C_3N_4, indicating that the separation and transfer efficiency of electrons was enhanced. Moreover, the EIS Nyquist plots arc radius of CN-BiS-2 was smaller than that of g-C_3N_4 (Fig. 9b), which could further confirm the higher separation and transfer efficiency of photogenerated electron as well as hole pairs.
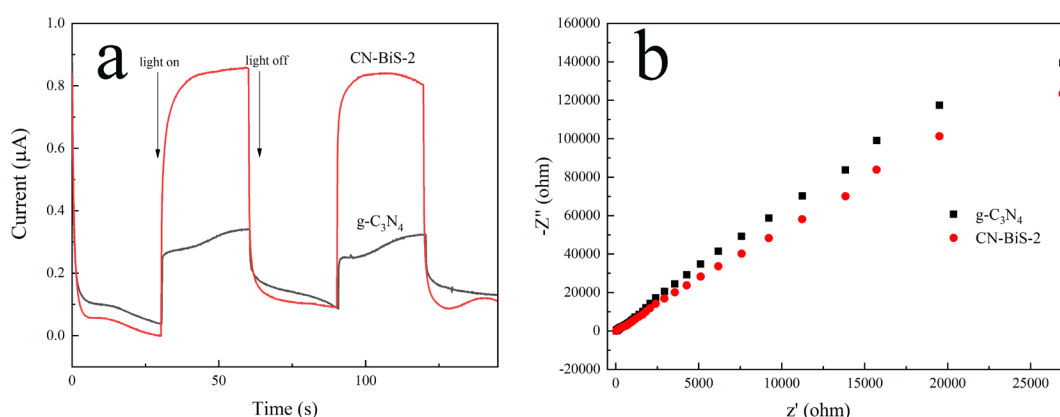

Fig. 9 Photocurrent response (a) and EIS Nyquist plots (b) of g-C_3N_4 and CN-BiS-2 in 0.1 M Na_2SO_4 solution

Afterwards, PL spectra were used to further determine the separation and transfer efficiency of photogenerated charge carriers. As shown in Fig. 10a, the CN-BiS-2 showed much lower PL spectra intensity than g-C_3N_4, illustrating that the introduction of Bi_2S_3 can restrain the recombination of photogenerated electron and hole pairs.

Then radical trapping experiments were also carried out to explore the main radicals in the photochemical reaction process of CN-BiS-2 (Fig. 10b). When IPA or

N$_2$ was added to the reaction system, the photocatalytic activity reduced, while the extent was minor. In contrast, KI had a distinct influence on the photocatalytic performance of CN-BiS-2, which meant that holes were the most important radicals during the photodegradation process of CN-BiS-2.

After that, ESR spectra were used to compare the effect of hydroxyl radicals and superoxide radicals of g-C$_3$N$_4$ and CN-BiS-2 (Figs. 10c and 10d). In a dark environment, neither g-C$_3$N$_4$ nor CN-BiS-2 showed obvious ESR signal. After light irradiation, both the samples had hydroxyl radical and superoxide radical ESR signal. The hydroxyl radical ESR spectra intensity and superoxide radical ESR spectra intensity of CN-BiS-2 were both stronger than that of g-C$_3$N$_4$, which indicated that CN-BiS-2 can provide more electrons and holes. As a result, more radicals were generated.
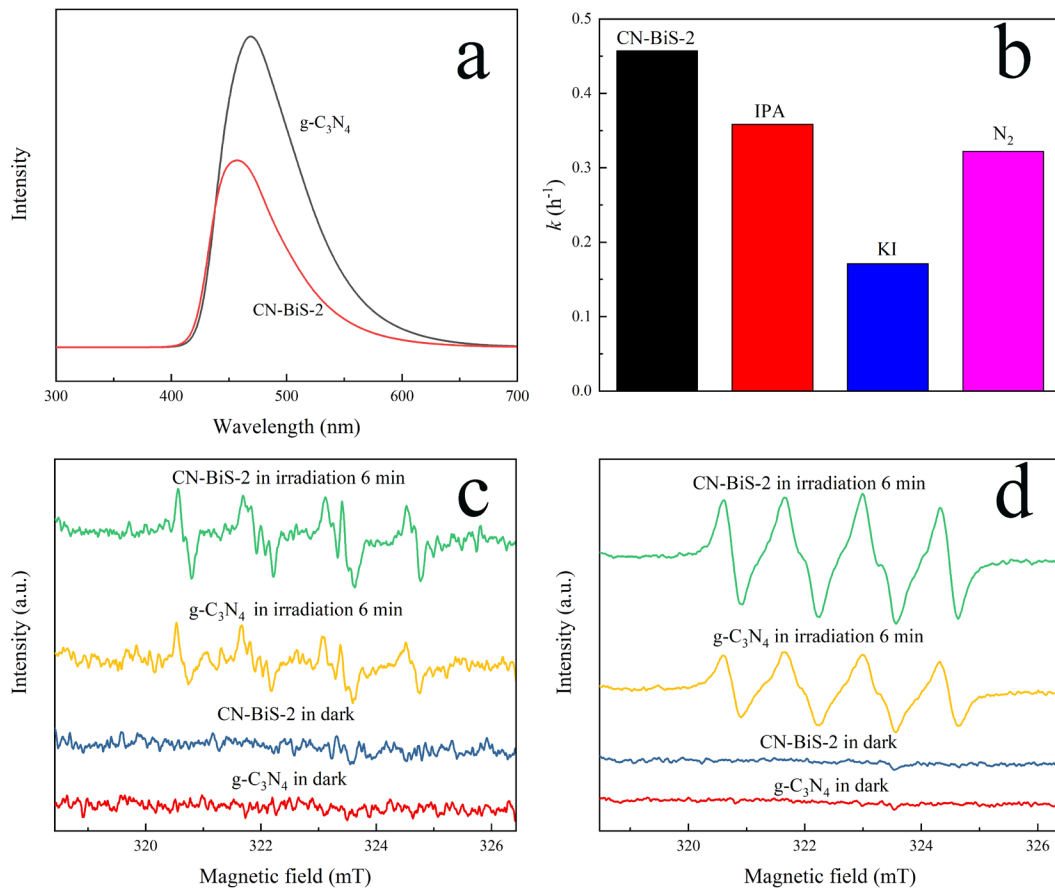
Fig. 10 Photoluminescence spectra of g-C$_3$N$_4$ and CN-BiS-2 (a); radical trapping experiment results of CN-BiS-2 during the photodegradation process of MB (b); ESR spectra of hydroxyl radicals (c) and superoxide radicals (d) trapped by DMPO.

Photothermal conversion materials can accumulate solar radiation energy and convert it to thermal energy. Under solar light irradiation, Bi$_2$S$_3$ can absorb light energy and improve its temperature.[49] Fig. 11 is the temperature-time curve of g-C$_3$N$_4$ and CN-BiS-2 under simulated solar light irradiation. The temperature of g-C$_3$N$_4$ and CN-BiS-2 both increased rapidly, and it gradually became stable. At 27 minutes, the temperature of CN-BiS-2 reached about 82.4 °C, while that of g-C$_3$N$_4$ was about 68.4 °C. These results indicated that the introduction of Bi$_2$S$_3$ is beneficial to the

photothermal conversion effect of CN-BiS-2, which can provide more energy to electrons and make them transfer much faster to vitally enhance photocatalytic reaction.[62, 63]
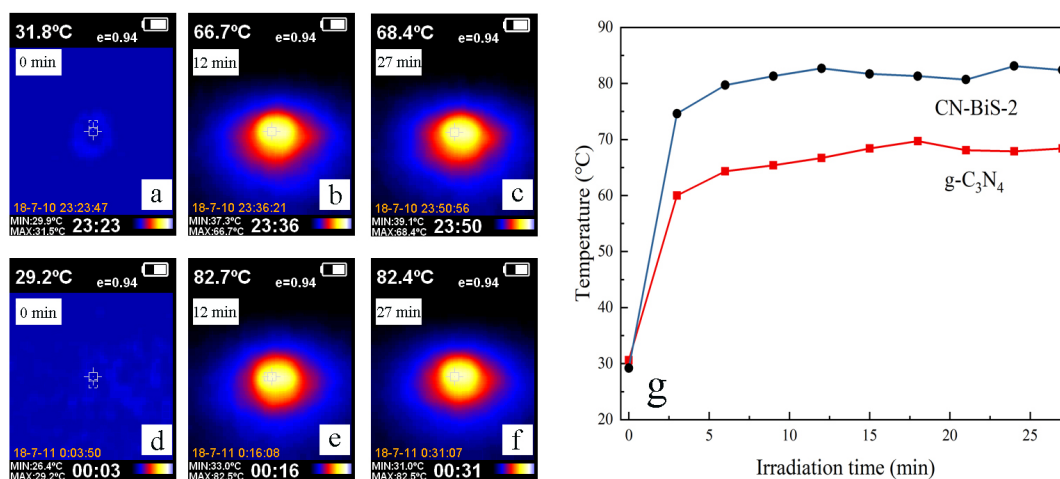

Fig. 11 Thermal images of g-C$_3$N$_4$ (a-c) and CN-BiS-2 (d-f) under simulated solar light irradiation for 0, 12 and 27 min; the temperature-time curve of g-C$_3$N$_4$ and CN-BiS-2 under simulated solar light irradiation in 27 min.

In brief, the UV-vis DRS of CN-BiS-2 had obvious red-shift and it can confirm the light utilization is greatly enhanced. The stronger photocurrent response, the smaller EIS Nyquist plots arc radius, and the lower intensity of PL all indicated the separation and transfer of photogenerated charge carriers was clearly improved. The results of trapping experiments concluded that the most important active species in the photodegradation process are holes. The hydroxyl radical ESR spectra intensity and superoxide radical ESR spectra intensity of CN-BiS-2 were both stronger than that of g-C$_3$N$_4$, which indicates that CN-BiS-2 can provide more electrons and holes, as a

result, more radicals are generated. Due to the photothermal effect of Bi_2S_3, the carrier mobility was enhanced, which was also important for the photocatalytic reaction.

Based on all the above results, a possible mechanism for why g-C_3N_4/Bi_2S_3 heterojunction showed better photocatalytic performance was proposed (Fig. 12). The conduction band (CB) and valence band (VB) of g-C_3N_4 are at −1.13 and +1.57 eV respectively.[24] The CB of Bi_2S_3 is 0.10 eV and its VB is +1.45 eV.[51] Generally, electrons carry negative charges and trend to migrate to more positive potential; holes carry positive charges and trend to migrate to more negative potential. Judging from the band structure of g-C_3N_4 and Bi_2S_3, electrons and holes both have the tendency to transfer to the CB and VB of Bi_2S_3, which may lead to reduction of the redox ability. As a result, g-C_3N_4 and Bi_2S_3 may not form a highly efficient heterojunction. However, when high-energy electrons are produced, this circumstance can be changed.[64, 65] Based on the results of photocurrent, EIS, PL and ESR, it can be concluded that the transfer and separation of photogenerated charge carriers are accelerated, besides the photocatalytic performance of CN-BiS-2 is 2.05 time as g-C_3N_4 and 4.42 times as Bi_2S_3. The gap between the VB top of Bi_2S_3 and the CB bottom of g-C_3N_4 is 2.58 eV, corresponding to the light energy of about 480 nm, which means that high-energy electrons of Bi_2S_3 excited by light shorter than 480 nm can energetically transfer to the CB of g-C_3N_4. The light range of xenon lamp we used is 200-1100 nm, indicating that the electrons on the VB of Bi_2S_3 can be excited to the maximum of -4.73 eV.

Firstly, under simulated sunlight irradiation, both g-C_3N_4 and Bi_2S_3 are excited; electrons can transfer to the CB and holes are produced on the VB. Electrons can react

with oxygen to produce superoxide radicals. Holes can react with water and produce hydroxyl radicals. Superoxide radicals, hydroxyl radicals and hole are all strong oxidative species in photocatalytic reactions. Due to the high energy of simulated sunlight, a lager quantity of high-energy electrons are produced, which can transfer to the CB of g-C_3N_4, at the same time holes can migrate from the VB of g-C_3N_4 to the VB of Bi_2S_3. As a result, the separation of photogenerated charge carriers is accelerated. Besides, the introduction of Bi_2S_3 greatly enhanced the light absorption both in the ultraviolet and visible light region (Fig. 8). Finally, the photothermal effect of Bi_2S_3 can provide more energy to electrons and make them transfer much faster. Based on the above results, the g-C_3N_4/Bi_2S_3 heterojunction materials exhibit better photocatalytic performance.
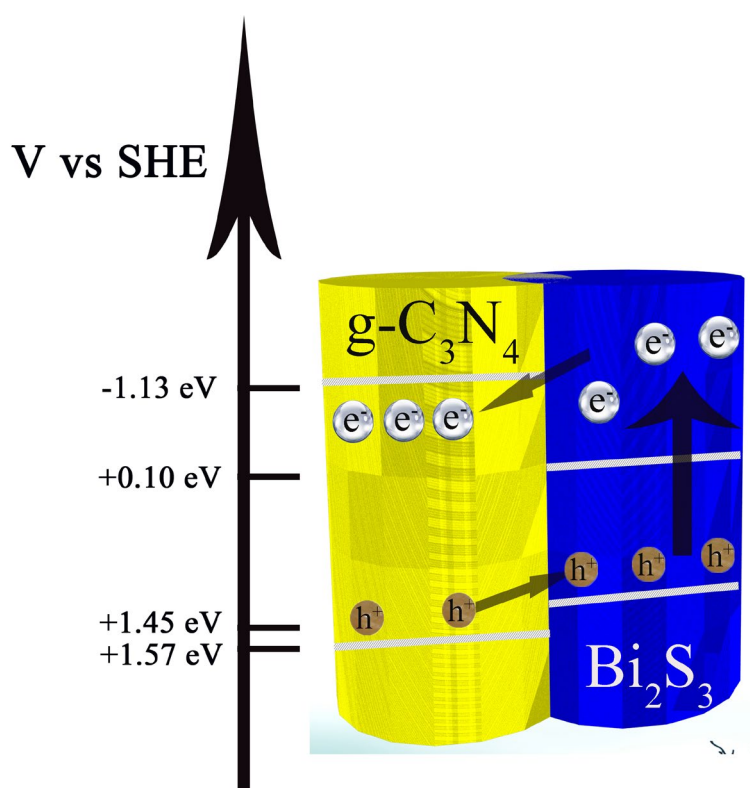

Fig. 12 Schematic diagram for possible charge separation in g-C_3N_4/Bi_2S_3 heterojunctions

4. Conclusion

In this work, a series of g-C$_3$N$_4$/Bi$_2$S$_3$ heterojunction materials with effective photocatalytic performance was constructed. The results of photocurrent, EIS, PL and ESR can confirm that transfer and separation of photogenerated charge carriers were promoted. The introduction of Bi$_2$S$_3$ can enhance the absorption of light energy and convert it to thermal energy, which can provide more energy to electrons and make them transfer much faster. Due to the high energy of simulated sunlight, a large quantity of high-energy electrons were produced, which can transfer to the CB of g-C$_3$N$_4$, at the same time holes can migrate from the VB of g-C$_3$N$_4$ to the VB of Bi$_2$S$_3$. As a result, the separation of photogenerated charge carriers is accelerated. The findings of this work provide a new facile way to develop highly efficient heterojunction photocatalysts via high-energy electrons and photothermal effect.

References

1. Y. Choi, M. S. Koo, A. D. Bokare, D. H. Kim, D. W. Bahnemann, W. Choi, *Environ. Sci. Technol.*, **2017**, 51, 3973-3981.

2.   S. G. Kumar, K. S. R. K. Rao, *Appl. Surf. Sci.*, **2017**, 391, 124-148.
3.   Y. Wang, H. Dai, J. Deng, Y. Liu, H. Arandiyan, X. Li, B. Gao, S. Xie, *Solid State Sci.*, **2013**, 24, 62-70.
4.   H. J. Lu, R. T. Wang, L. H. Zhang, D. M. Chen, Q. Hao, C. Ma, W. Q. Yao, *Russ. J. Phys. Chem. A*, **2018**, 92, 2075-2080.
5.   K. M. Reza, A. S. W. Kurny, F. Gulshan, *Appl. Water Sci.*, **2017**, 7, 1569-1578.
6.   Z. X. Zhao, H. X. Dai, J. G. Deng, Y. X. Liu, Y. Wang, X. W. Li, G. M. Bai, B. Z. Gao, C. T. Au, *J. Environ. Sci.*, **2013**, 25, 2138-2149.
7.   A. Fujishima, K. Honda, *Nature*, **1972**, 238, 37-38.
8.   W.-K. Jo, S. Kumar, M. A. Isaacs, A. F. Lee, S. Karthikeyan, *Appl. Catal. B-Environ.*, **2017**, 201, 159-168.
9.   K. M. Lee, C. W. Lai, K. S. Ngai, J. C. Juan, *Water Res.*, **2016**, 88, 428-448.
10.   S. Liu, M. Y. Zhao, Z. T. He, Y. Zhong, H. Ding, D. M. Chen, *Chin. J. Catal.*, 2019, **40**, 446-457.
11.   Z. Zou, J. Ye, K. Satama. H. Arakawa, *Nature*, **2001**, 414, 625-627.
12.   T. Chen, Q. Hao, W. J. Yang, C. L. Xie, D. M. Chen, C. Ma, W. Q. Yao, Y. F. Zhu, *Appl. Catal. B-Environ.*, **2018**, 237, 442-448.
13.   Q. Hao, R. Wang, H. Lu, C. a. Xie, W. Ao, D. Chen, C. Ma, W. Yao, Y. Zhu, *Appl. Catal. B-Environ.*, **2017**, 219, 63-72.
14.   H. Lu, Q. Hao, T. Chen, L. Zhang, D. Chen, C. Ma, W. Yao, Y. Zhu, *Appl. Catal. B-Environ.*, **2018**, 237, 59-67.
15.   S. Kohtani, M. Koshiko, A. Kudo, K. Tokumura, Y. Ishigaki, A. Toriba, K. Hayakawa, R. Nakagaki, *Appl. Catal. B-Environ.*, **2003**, 46, 573-586.
16.   S. Dong, Y. Cui, Y. Wang, Y. Li, L. Hu, J. Sun and J. Sun, *Chem. Eng. J.*, **2014**, 249, 102-110.
17.   Q. Wang, J. Lian, Q. Ma, S. Zhang, J. He, J. Zhong, J. Li, H. Huang, B. Su, *Catal. Today*, **2017**, 281, 662-668.
18.   Y.-J. Yuan, Z. Li, S. Wu, D. Chen, L.-X. Yang, D. Cao, W.-G. Tu, Z.-T. Yu, Z.-G. Zou, *Chem. Eng. J.*, **2018**, 350, 335-343.
19.   R. Suresh, K. Giribabu, R. Manigandan, R. V. Mangalaraja, J. Yanez Solorza, A. Stephen, V. Narayanan, *Solid State Sci.*, **2017**, 68, 39-46.
20.   K. Sekizawa, S. Sato, T. Arai, T. Morikawa, *ACS Catalysis*, **2018**, 8, 1405-1416.
21.   W. Zhang, Z. Zhao, F. Dong, Y. Zhang, *Chin. J. Catal.*, **2017**, 38, 372-378.
22.   Q. Hao, T. Chen, R. Wang, J. Feng, D. Chen, W. Yao, *J. Clean. Prod.*, **2018**, 197, 1222-1230.
23.   Q. Hao, X. X. Niu, C. S. Nie, S. M. Hao, W. Zou, J. M. Ge, D. M. Chen, W. Q. Yao, *Phys. Chem. Chem. Phys.*, **2016**, 18, 31410-31418.
24.   Q. Hao, S. M. Hao, X. X. Niu, X. Li, D. M. Chen, H. Ding, *Chin. J. Catal.*, **2017**, 38, 278-286.
25.   J. Q. Wen, J. Xie, X. B. Chen, X. Li, *Appl. Surf. Sci.*, **2017**, 391, 72-123.
26.   D. Masih, Y. Ma, S. Rohani, *Appl. Catal. B-Environ.*, **2017**, 206, 556-588.
27.   Y. H. Fu, W. Liang, J. Q. Guo, H. Tang, S. S. Liu, *Appl. Surf. Sci.*, **2018**, 430, 234-242.

28.   Q. Xu, B. Zhu, C. Jiang, B. Cheng, J. Yu, *Solar Rrl*, **2018**, 2, 1800006.

29.   W. J. Jiang, H. Wang, X. D. Zhang, Y. F. Zhu, Y. Xie, *Sci. China-Chem.*, **2018**, 61, 1205-1213.

30.   D. Chen, K. Wang, W. Hong, R. Zong, W. Yao, Y. Zhu, *Appl. Catal. B-Environ.*, 2015, **166**, 366-373.

31.   X. J. Wang, Q. Wang, F. T. Li, W. Y. Yang, Y. Zhao, Y. J. Hao, S. J. Liu, *Chem. Eng. J.*, **2013**, 234, 361-371.

32.   Z. W. Tong, D. Yang, T. X. Xiao, Y. Tian, Z. Y. Jiang, *Chem. Eng. J.*, **2015**, 260, 117-125.

33.   H. P. Li, J. Y. Liu, W. G. Hou, N. Du, R. J. Zhang, X. T. Tao, *Appl. Catal. B-Environ.*, **2014**, 160, 89-97.

34.   F. T. Li, Y. Zhao, Q. Wang, X. J. Wang, Y. J. Hao, R. H. Liu, D. S. Zhao, *J. Hazard. Mater.*, **2015**, 283, 371-381.

35.   F. J. Zhang, F. Z. Xie, S. F. Zhu, J. Liu, J. Zhang, S. F. Mei, W. Zhao, *Chem. Eng. J.*, **2013**, 228, 435-441.

36.   F. Chen, H. Yang, X. Wang, H. Yu, *Chin. J. Catal.*, **2017**, 38, 296-304.

37.   P. Wang, S. Xu, F. Chen, H. Yu, *Chin. J. Catal.*, **2019**, 40, 343-351.

38.   N. C. Zheng, T. Ouyang, Y. B. Chen, Z. Wang, D. Y. Chen, Z. Q. Liu, *Catal. Sci. Technol.*, **2019**, 9, 1357-1364.

39.   R. B. Wei, Z. L. Huang, G. H. Gu, Z. Wang, L. X. Zeng, Y. B. Chen, Z. Q. Liu, *Appl. Catal. B-Environ.*, **2018**, 231, 101-107.

40.   D. S. Wang, C. H. Hao, W. Zheng, X. L. Ma, D. R. Chu, Q. Peng, Y. D. Li, *Nano Res.*, **2009**, 2, 130-134.

41.   Y. Bessekhouad, D. Robert, J. Weber, *J. Photoch. Photobio. A*, **2004**, 163, 569-580.

42.   X. Gao, H. B. Wu, L. Zheng, Y. Zhong, Y. Hu, X. W. Lou, *Angew. Chem. Int. Edit.*, **2014**, 53, 5917-5921.

43.   G. Konstantatos, L. Levina, J. Tang, E. H. Sargent, *Nano Lett.*, **2008**, 8, 4002-4006.

44.   G. Chen, Y. Yu, K. Zheng, T. Ding, W. Wang, Y. Jiang, Q. Yang, *Small*, **2015**, 11, 2848-2855.

45.   K. L. Ai, Y. L. Liu, J. H. Liu, Q. H. Yuan, Y. Y. He, L. H. Lu, *Adv. Mater.*, **2011**, 23, 4886-4891.

46.   P. Boudjouk, M. P. Remington, D. G. Grier, B. R. Jarabek, G. J. McCarthy, *Inorg. Chem.*, **1998**, 37, 3538-3541.

47.   X. L. Yu, C. B. Cao and H. S. Zhu, *Solid State Commun.*, **2005**, 134, 239-243.

48.   Z. Guo, S. Zhu, Y. Yong, X. Zhang, X. Dong, J. Du, J. Xie, Q. Wang, Z. Gu, Y. Zhao, *Adv. Mater.*, **2017**, 29, 1704136.

49.   Z. Xiao, C. Xu, X. Jiang, W. Zhang, Y. Peng, R. Zou, X. Huang, Q. Liu, Z. Qin, J. Hu, *Nano Res.*, **2016**, 9, 1934-1947.

50.   X. Zhou, S. Y. Yao, Y. M. Long, Z. S. Wang, W. F. Li, *Mater. Lett.*, **2015**, 145, 23-26.

51.   D. D. Chen, J. Z. Fang, S. Y. Lu, G. Y. Zhou, W. H. Feng, F. Yang, Y. Chen, Z. Q. Fang, *Appl. Surf. Sci.*, **2017**, 426, 427-436.

52.   J. Yin, Z. Y. Wu, M. Fang, Y. Xu, W. J. Zhu, C. Li, *J. Chin. Chem. Soc.*, **2018**, 65, 1044-1052.

53.   P. Niu, L. L. Zhang, G. Liu, H. M. Cheng, *Adv. Funct. Mater.*, **2012**, 22, 4763-4770.

54.   L. F. Lundegaard, E. E. Makovicky, T. Boffa-Ballaran, T. Balic-Zunic, *Phys. Chem. Miner.*, **2005**, 32, 578-584.

55.   H. Jung, C. M. Park, H. J. Sohn, *Electrochim. Acta*, **2011**, 56, 2135-2139.

56.   W. G. Ma, D. X. Han, M. Zhou, H. Sun, L. N. Wang, X. D. Dong, L. Niu, *Chem. Sci.*, **2014**, 5, 3946-3951.

57.   Q. Y. Lin, L. Li, S. J. Liang, M. H. Liu, J. H. Bi, L. Wu, *Appl. Catal. B-Environ.*, **2015**, 163, 135-142.

58.   J. R. Holst, E. G. Gillan, *J. Am. Chem. Soc.*, **2008**, 130, 7373-7379.

59.   B. Jurgens, E. Irran, J. Senker, P. Kroll, H. Muller, W. Schnick, *J. Am. Chem. Soc.*, **2003**, 125, 10288-10300.

60.   J. Grigas, E. Talik, V. Lazauskas, *Phys. Status Solidi B-Basic Res.*, **2002**, 232, 220-230.

61.   F. M. Huang, L. Chen, H. L. Wang, Z. C. Yan, *Chem. Eng. J.*, **2010**, 162, 250-256.

62.   Z. Gan, X. Wu, M. Meng, X. Zhu, L. Yang, P. K. Chu, *ACS Nano*, **2014**, 8, 9304-9310.

63.   R. T. Wang, Q. Hao, J. R. Feng, G. C. Wang, H. Ding, D. M. Chen, B. J. Ni, *J. Alloy. Compd.*, **2019**, 786, 418-427.

64.   M. Z. Xie, X. D. Fu, L. Q. Jing, P. Luan, Y. J. Feng, H. G. Fu, *Adv. Energy Mater.*, **2014**, 4, 1300995.

65.   M. Humayun, Y. Qu, F. Raziq, R. Yan, Z. Li, X. Zhang and L. Jing, *Environ. Sci. Technol.*, **2016**, 50, 13600-13610.